

# Measurement of the atmospheric limit to narrow-angle interferometric astrometry using the Mark III stellar interferometer

M. M. Colavita

Jet Propulsion Laboratory, California Institute of Technology, 4800 Oak Grove Dr., Pasadena, CA 91109, USA

Received date; accepted date

**Abstract.** Measurements were made with the Mark III stellar interferometer in order to verify predictions for the accuracy of very-narrow-angle interferometric astrometry. The Mark III was modified to observe simultaneously on its 12-111 baseline the phase of the fringe packets of the primary and secondary of the 3.3" binary star  $\alpha$  Gem. The residuals of the phase difference between primary and secondary were analyzed for 6 data segments taken over two nights. Examination of the Allan variances of the data out to a measurement limit of 8 min indicate that the error is white, as predicted. The mean fluctuations of the residuals corresponds to an astrometric accuracy of  $21 \mu\text{as}/\sqrt{t}$ , which is in good agreement with the predictions of atmospheric models. An accurate separation for  $\alpha$  Gem was also determined:  $3.281'' \pm 0.01''$  at position angle  $73.23^\circ \pm 0.15^\circ$  for 1992.9589.

**Key words:** Atmospheric effects - instrumentation: interferometers - Methods: observational - Techniques: interferometric Astrometry - Stars: alpha Gem

## 1. Introduction

Atmospheric turbulence is the limiting factor for all ground-based astrometric measurements. While differential measurements have smaller errors than absolute measurements, and also exhibit a white-noise error power spectrum, they are still limited by turbulence. The detailed error behavior for a differential measurement depends on the relationship among the star separation, the mean atmospheric height, and the instrument baseline. In particular, it is convenient to define the isokinetic angle  $\theta_k$  as  $B/\bar{h}$ , where  $B$  is the instrument baseline (or telescope diameter) and  $\bar{h}$  is a mean atmospheric height. For star separations  $\theta > \theta_k$  - the usual narrow-angle regime - the error  $\epsilon_{\Delta\theta}$  in a differential measurement is dependent only weakly on the star separation and the instrument baseline. However, for  $\theta < \theta_k$ , the error is strongly dependent on both separation and baseline length. More precisely, in terms of a standard infinite-outer-scale Kolmogorov atmospheric model, the variance in a differential measurement can be written (Lindgren 1980; Shao & Colavita 1992)

$$\epsilon_{\Delta\theta}^2 \simeq 5.25 \left[ \frac{B^{-4/3} \theta^2 \int dh C_n^2(h) h^2 W^{-1}(h)}{\theta^{2/3} \int dh C_n^2(h) h^{2/3} W^{-1}(h)} \right] t^{-1},$$

$$\left[ \begin{array}{l} 0 < \theta_k, t \gg B/\bar{W} \\ \theta \gg \theta_k, t \gg (\theta \bar{h})/\bar{W} \end{array} \right]. \quad (1)$$

where  $C_n^2(h)$  is the turbulence profile as a function of height,  $W$  is the wind speed, and  $t$  is the integration time. This expression is plotted in Fig. 1 using atmospheric parameters appropriate to Mauna Kea, Hawaii.

Send offprint requests to:

**Fig. 1.** Differential astrometric error for several baseline lengths using measured Mauna Kea turbulence profiles and an integration time of 1 h; from Shao & Colavita (1992)



The desirable behavior in the regime  $\theta < \theta_k$ , where the error standard deviation is linear with star separation and inversely proportional to  $(\text{baseline})^{2/3}$ , can be exploited with long-baseline infrared interferometry (Shao & Colavita 1992). In particular, with observations at  $2.2 \mu\text{m}$ , phase referencing to synthesize long coherent integration times in order to select faint, nearby reference stars, and with long baselines to reduce atmospheric and photon noise errors, differential measurements with an accuracy of tens of microarcseconds ( $\mu\text{as}$ ) per  $\sqrt{h}$  should be possible. Such accuracy would allow for the astrometric detection of exoplanets from the ground.

While measurements of the behavior of differential measurements in the regime  $\theta > \theta_k$  exist and are consistent with Eq. (1) (Han 1989), quantitative measurements of astrometric behavior in the regime  $\theta < \theta_k$  are sparse. Measurements by Gatewood (1991) using trail plates from the 3.6-m CFHT telescope on Mauna Kea confirmed the improved astrometric behavior which occurs for small star separations;<sup>1</sup> however, the noise floor of the measurements prevented a quantitative assessment of the performance for  $\theta \ll \theta_k$ . The objective of the present investigation was to confirm Eq. (1) in the very-narrow-angle regime with respect to overall scale factor and the predicted white-noise behavior for one set of baseline and star-separation parameters. To this end a set of observations were conducted using the Mark III stellar interferometer on Mt. Wilson.

Section 2, below, describes the instrument configuration used in this experiment. Sections 3 and 4 describe the observations and the data processing. Finally, Sects. 5 and 6 provide a discussion of the experimental results and some conclusions.

## 2. Instrument configuration

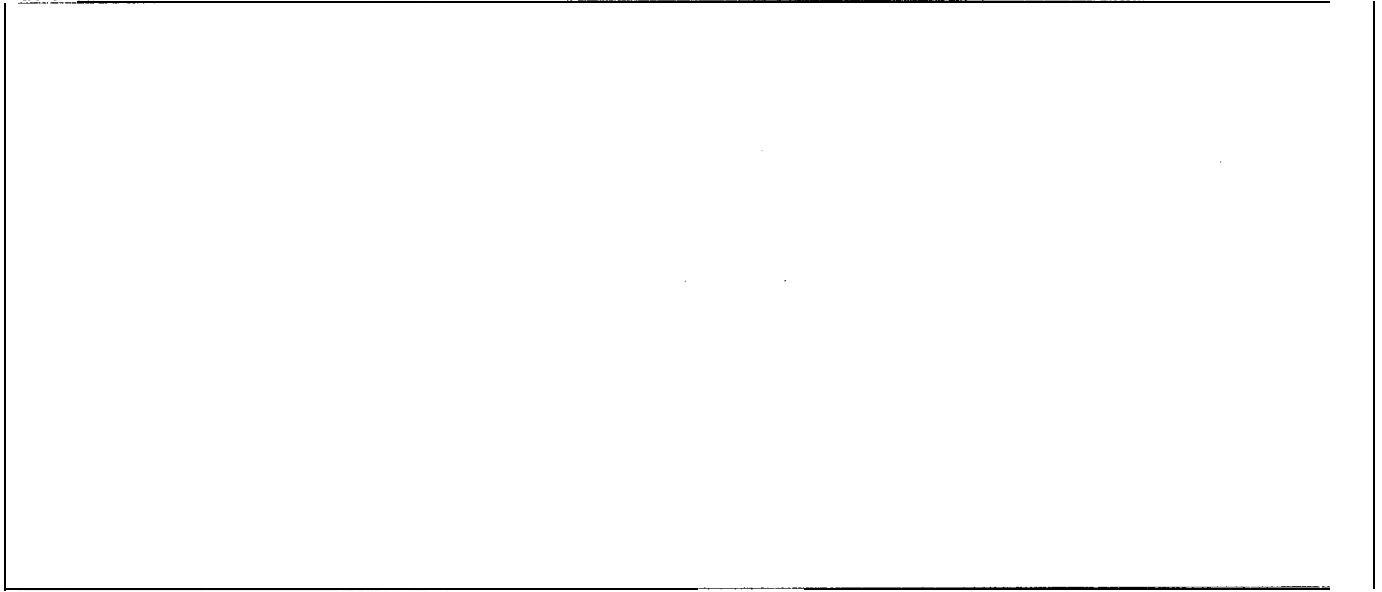
The measurements described below were made with the Mark III stellar interferometer, a long-baseline optical interferometer on Mt. Wilson (Shao et al. 1988a). The Mark II I was modified to simultaneously observe, on separate channels, the fringe phase from two stars separated by several arc seconds. The target for these measurements was the binary star  $\alpha$  Gem.

To properly exploit the atmospheric behavior in the very-narrow-angle regime, an interferometer should incorporate a dual-beam feed at each aperture to separate the light from individual stars in the field and route it to separate optical trains and beam combiners to simultaneously measure the fringe phases. However, with a single-beam instrument like the Mark III, a simultaneous differential measurement can be accomplished by choosing a pair of stars within the subaperture beam and separating them in delay space. In particular, rather than choosing a very-narrow-bandwidth filter as would be appropriate for synthesis imaging of the entire field, wider filters are used such that the fringe packets from the two stars do not overlap. The pupil is then partitioned into subpupils with separate detectors and different delays so that simultaneous phase measurements can be made for the two stars. The disadvantage of this scheme is the loss of light due to pupil division and the extra noise resulting from the incoherent background from the second star in each channel. However, for the purposes of this experiment, the resulting restriction to bright sources is not a problem.

<sup>1</sup> Gatewood refers to the region of improved performance as the isokinetic patch; thus the description of  $\theta_k$  as the isokinetic angle.

Figure 2 illustrates the instrument configuration used for these measurements. In normal operation of the Mark III light from the north and south arms is routed through optical delay lines and combined at a beamsplitter. The beamsplitter outputs are divided into a wideband channel for tracking the white-light fringe and three narrowband channels for precise amplitude measurements. Pathlength (temporal) modulation introduced by one delay line, in conjunction with binning of the photon counts, is used to measure the fringe parameters in each channel at a 4-ns rate. The fringe phase from the white-light channel is used in real time to control the position of the second delay line in order to track the atmospheric phase fluctuations.

Fig. 2. Optical schematic of the Mark III interferometer as configured for these measurements and the pupil geometry which was used



For the measurements described here, the instrument was modified as shown in the figure by dividing the 5-cm-diameter fringe-tracking pupil into adjacent semicircular subpupils and using separate detectors for each. The light from the primary subpupil was divided into three spectral channels: a wideband channel (no. 1), N560-1000 nm, for fringe tracking in the usual way, and two narrowband channels (nos. 4 & 3), one at 700 nm, 25-rim wide, and a second at 500 nm (the light from this channel was not used here). The light from the secondary subpupil was detected on a single channel (no. 2) also using a 700 nm, 25-rim wide filter. For this experiment channels 1 and 2 used high-sensitivity silicon photon-counting avalanche photodiode detectors (APDs), while the other channels used GaAs photomultiplier tubes.

To simultaneously detect the fringe packet from the secondary star in channel 2 while fringe tracking on the primary star, a pair of rotating glass plates were inserted into the secondary subpupil. As shown in the figure these plates act as differential delay lines to modify the total delay to the proper value needed for the secondary star. The plates were 12.7-mm-thick BK7, shaped to minimize obscuration of the annular portion of the pupil used for angle tracking. For this experiment, which had the secondary star north of the primary star, the plate in the south arm was adjusted normal to the beam, while the tilt of the plate in the north arm was adjusted using a motorized translator. As a function of rotation angle  $\Theta$ , the delay  $x$  introduced by each plate is given as

$$x = \frac{1 (n_g - n_a \cos(\Theta - \Theta'))}{\cos \Theta'} \quad (2)$$

where  $n_g$  and  $n_a$  are the indices of the glass and air, 1 is the plate thickness, and  $\Theta'$  is the internal angle  $\sin^{-1}(n_a \sin \Theta / n_g)$ .

The coherence length of the narrowband filters used in the experiment is  $\sim 20 \mu\text{m}$ , which establishes the accuracy with which the differential delay must be set. In a practical dual-beam interferometer the differential delay would be monitored by a separate metrology system and would be adjusted continuously to maintain coherence. For this experiment, which did not incorporate additional metrology beyond that used on the main delay lines, the rotating

plate was moved to fixed positions. The secondary fringe was then allowed to drift through the coherence length of its filter with earth rotation as the fringe on the primary was tracked by the main delay line. Using its translator, the delay introduced by the rotating plate could be set to  $\sim 5 \mu\text{m}$ .

The required differential delay is easily determined from the standard expression for the overall delay  $x: x = B \cdot \hat{s}$ , where  $B$  is the baseline vector and  $\hat{s} = \hat{x} \cos \delta \cos H - \hat{y} \cos \delta \sin H + \hat{z} \sin \delta$  is the source unit vector in equatorial coordinates ( $H = \text{HA}$ ,  $\delta = \text{decl.}$ ). For a small separation between stars of  $\Delta\delta$  and  $\Delta\alpha$  in declination and right ascension, the differential delay is given by (cf. Thompson et al. 1986)

$$\Delta x = B \cdot \Delta \hat{s}, \quad (3)$$

where

$$\begin{aligned} \Delta \hat{s} \simeq & \hat{x}(-\sin \delta \cos H \Delta \delta + \cos \delta \sin H \Delta \alpha) \\ & + \hat{y}(\sin \delta \sin H \Delta \delta + \cos \delta \cos H \Delta \alpha) \\ & + \hat{z}(\cos \delta \Delta \delta). \end{aligned} \quad (4)$$

For the small separations of the experiment, this is an excellent approximation.

### 3. Observations

The instrument configuration used for these measurements imposes several constraints on the target stars: a) the primary star needs to be bright, as the fringe-tracking aperture is half the normal size, b) the magnitude difference between the primary and secondary needs to be large enough that there is no ambiguity between fringe packets for the white-light tracker, but small enough that the background from the bright star doesn't overwhelm the signal from the dim star, c) the difference in delay between stars needs to be larger than the coherence length of the narrowband filters to prevent overlap of the fringe packets, and d) the star separation needs to be within the isoplanatic patch to allow the primary to serve as a phase and angle-tracking reference for the secondary.

The visual binary  $\alpha$  Gem (ADS 6175; HR 2891, 2890; R. A. (2000)  $07^h 34^m 37^s$ , decl.  $+31^\circ 53' 24''$ ;  $m_1 = 1.94$ ,  $m_2 = 2.92$ ) (cf. Hirshfeld & Sinnott 1985) meets the requirements above and was used as the target for these observations. As the two components are of similar spectral type (A1V and A2V), the magnitude difference at 700 nm should be close to the visual difference. For these measurements the approximate binary separation was  $3.3''$  at a position angle of  $75^\circ$ ; as  $\alpha$  Gem has a period of at least 400 y, orbital motion during the observations can be ignored.

The 12-m N-S astrometric baseline of the Mark III was used for these measurements. Measurements were conducted over three nights in 1992: 9 Dec., 16 Dec., and 17 Dec. The first night was used for coarse astrometry and calibration of the differential delay; the data presented here are from the last two nights. These data consist of six segments, each longer than 15 min. They are delimited by changes in the fixed differential delay or by gaps in the data recording due to media changes. The basic observational parameters of these data segments are given in cols. 2-4 of table 1, and are also shown in Fig. 3, which plots the squared visibility amplitude ( $V$ ) on the secondary channel as a function of time as earth rotation sweeps the secondary fringe through the coherence length of the narrowband filter; the symbols on the graph indicate changes in the differential delay introduced by rotating the plate in the north arm to a new position.

Fig. 3. Squared visibility amplitude ( $V$ ) vs. time for the two nights analyzed here. The horizontal lines and letters identify the six segments analyzed in detail. The symbols indicate the times at which the differential delay was changed

Table 1. Summary of observations

(1) Segment	(2) UT date	(3) start time (h)	(4) duration (min)	(5) num pts (4 s)	(6) ZA (deg)	(7) $\sigma_x$ ( $\mu$ m)	(8) $r_0$ @0.55 $\mu$ m (cm)	(9) seeing (arcsec)	(10) $\theta_0$ (arcsec)
A	16 Dec 92	8.37	40.4	267	12.5	8.6	15.5	0.73	2.75
B	16 Dec 92	9.77	37.8	392	5.1	7.7	17.6	0.64	3.63
C	17 Dec 92	6.83	47.4	595	30.9	6.0	23.7	0.48	2.57
D	17 Dec 92	7.69	28.8	324	22.4	6.7	20.8	0.55	2.97
E	17 Dec 92	8.18	17.5	240	17.3	6.0	23.8	0.48	2.98
F	17 Dec 92	8.59	35.8	356	10.6	6.0	23.9	0.47	2.64
c1	17 Dec 92	5.86	3.1	33	47.3	8.0	17.0	0.67	-
C2	16 Dec 92	11.60	44.0	312	27.3	8.6	15.5	0.73	-

Table 2. Summary of measurements

(1) segment	(2) $N_p$ (4 ms)	(3) $V_p^2$	(4) SN (4 ms)	(5) $R_p^2 N_s$ (4 ms)	(6) $V_s^2$	(7) $SNR_s^2$ (4 ms)	(8) $I_d^2$	(9) $SNR_d^2$ (4 s)	(10) $\sigma_{PN}$ $\mu$ m(4 s)	(11) $\sigma_{\Delta x, A}$ $\mu$ m(4 s)	(12) $\sigma_{\Delta x, A}^2$ $\mu$ m(4 s)	(13) $\epsilon_{\Delta \theta}$ $\mu$ as/ $\sqrt{h}$
A	15.0	0.131	0.79	68.4	0.023	0.63	-0.103	15.2	0.029	0.051	0.043	24.6
B	16.9	0.144	0.98	67.2	0.021	0.58	0.191	30.4	0.020	0.033	0.026	14.9
C	18.3	0.219	1.62	56.8	0.031	0.72	0.085	22.9	0.023	0.048	0.042	24.3
D	18.1	0.221	1.62	55.7	0.012	0.28	0.126	14.5	0.029	0.050	0.041	23.4
E	19.4	0.229	1.81	59.5	0.019	0.45	0.127	24.3	0.023	0.038	0.031	17.8
F	19.1	0.214	1.66	58.7	0.035	0.84	0.091	28.3	0.021	0.045	0.040	23.2
C1	17.0	0.192	1.32	55.8	0.083	1.88	0.448	213.0	0.008	0.016	0.014	-
C2	18.4	0.158	1.18	61.9	0.003	0.07	0.480	11.8	0.032	0.041	0.025	-

#### 4. Data processing

As mentioned above, the Mark 111 uses pathlength modulation with 4 time bins to measure the fringe parameters. From the photon counts for each time bin, the quadratures  $X$  and  $Y$  and total photon count  $N$  per frame are determined for each of the 4 spectral channels. These data, plus the position of the laser-monitored delay line, are recorded every 4 ms when the instrument is locked on the white-light fringe.

From these data the square of the fringe visibility in the primary and secondary 700-11111 narrowband channels,  $V_p^2$  and  $V_s^2$ , is estimated with the usual unbiased estimator (Shao et al. 1988b)

$$V^2 = (\pi^2/2) \langle X^2 + Y^2 - N \rangle / \langle N \rangle^2, \quad (5)$$

where the indicated averaging is over  $M$  frames. For this experiment  $M=1000$  4-ms frames were used for a nominal intermediate integration time (for contiguous data) of 4 s. These fringe visibilities are reduced from unity by several factors: systematic instrumental effects, atmospheric turbulence, the finite diameter of the source, dark count (uncorrected in the expression above, but small), and the (incoherent) background from the other star. In particular, if we lump all but the last term into calibration constants  $V_{cp}^2$  and  $V_{cs}^2$ , the expected values for  $V^2$  are

$$\begin{aligned} V_p^2 &= V_{cp}^2 [R/(R+1)]^2 \\ V_s^2 &= V_{cs}^2 [1/(R+1)]^2, \end{aligned} \quad (6)$$

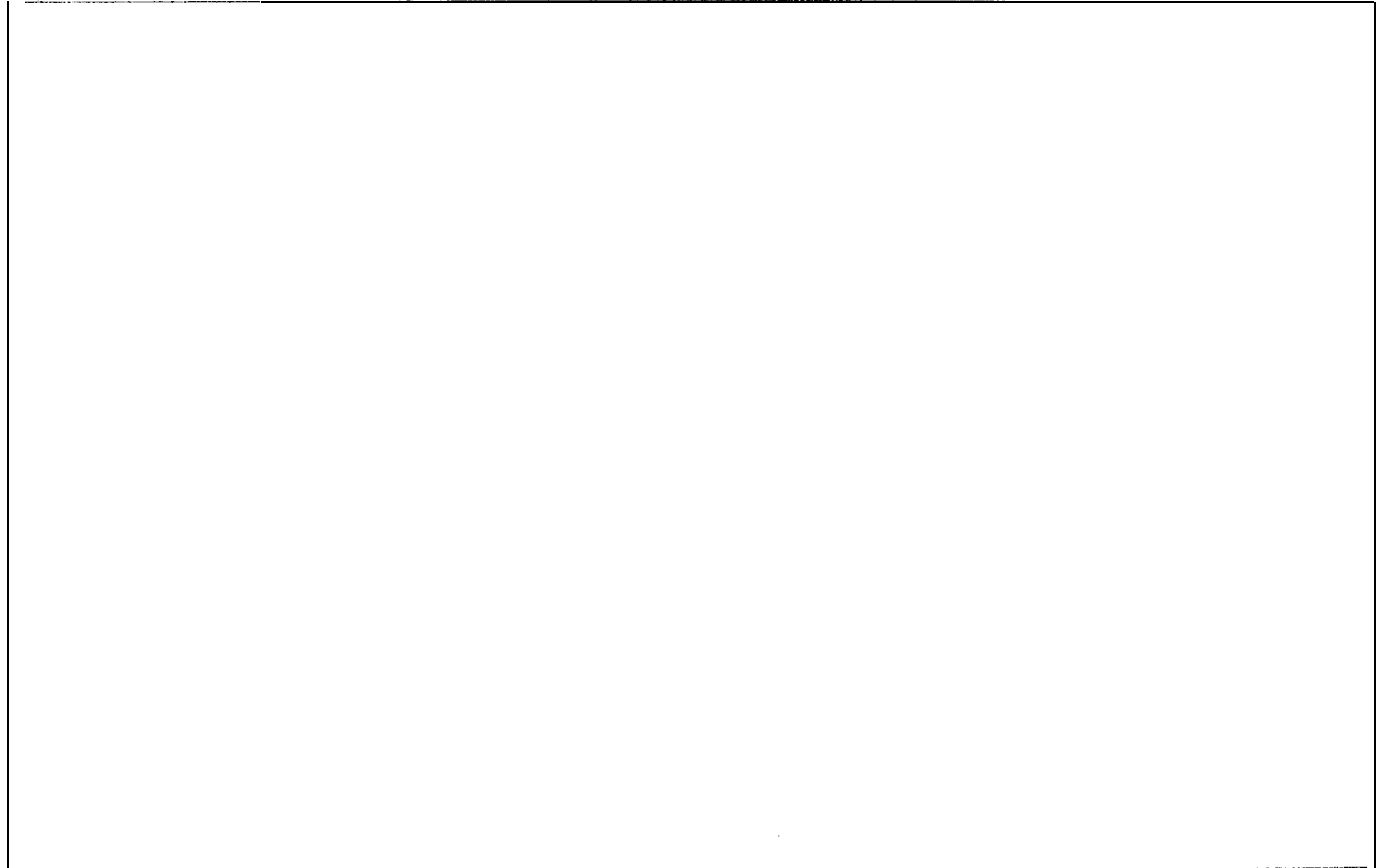
where  $R (>1)$  is the intensity ratio of the binary. For  $\alpha$  Gem,  $R=2.47$ , so the reductions in  $V^2$  beyond the ordinary calibrations are 0.51 and 0.083 for the primary and the secondary at the peak of their coherence functions. Without attempting to be particularly quantitative, the calibration constants  $V_c^2$  for these data are in the range 0.25-0.50, with the lower end of the range appropriate for the first night. These values are smaller than normally encountered with the

Mark 111 for quantitative visibility measurements because of the use of the off-axis apertures described above, which are more sensitive to guiding errors and residual system aberrations than the normal 2.5-cm centered apertures used for the narrowband channels. Columns 2-7 of Table 2 summarize  $N$  and  $V^2$  for the data. The entries denoted  $\text{SNR}^2$  are the square of the signal-to-noise ratio in 4 ms, calculated as  $\text{SNR}^2 = (4/\pi^2)NV^2$ ; in the photon-rich domain, the variance of a phase measurement is given as  $1/\text{SNR}^2$ . The much higher photon count in the secondary channel is attributable to the high-quantum-efficiency APD detector.

The fundamental observable for this experiment is the phase difference  $\Delta\phi = \phi_1 - \phi_2$  between the primary and secondary components (or  $Ax = k^{-1}\Delta\phi$ ,  $k = 2\pi/\lambda$ ,  $\lambda =$  wavelength). However, as inspection of Table 2 indicates, the SNR per 4 ms in the narrowband channels is inadequate to provide an unbiased phase estimate on that time scale. Thus some sort of phase referencing, exploiting the isoplanatic separation of the binary components, is needed to increase the SNR before calculating the phase from the quadrature. Ordinarily, one would phase reference the narrowband channels to the wideband primary channel. However, as the SNR in the narrowband primary channel is  $\approx 1$ , there is little SNR penalty in phase referencing the narrowband secondary channel directly to the narrowband primary channel, and the phase difference computed in this fashion was used here. The appendix provides details of computing the phase difference, as well as the properties of the phase-difference estimator.

Like the visibilities, the difference phasors were averaged coherently for 1000 4-ns frames. As shown in Fig. 4, which illustrates the processing for segment C, the estimated phase wraps over an interval of 700 nm as the secondary fringe sweeps through the coherence length of the filter. The chosen coherent integration time yields residual errors much smaller than wrapping interval so that the data can be unwrapped without ambiguity. In addition, at a 4 s integration time, the knee of the equivalent low-pass filter falls below the baseline cutoff frequency  $W/B$  in the phase-difference power spectrum, below which the spectrum should be white.

fig. 4. Intermediate outputs in the processing of segment C



Only minor editing of the data was performed at this stage; no editing was done on the raw quadrature or photon counts. In this experiment, in which the differential delay line moves only in steps, so that the phase difference varies

continuously, an excessively long intermediate integration time will blur the phase difference and thus reduce its SNR. More precisely, assuming a linear phase change  $(\Delta\phi)_{\max}$  during the integration, the SNR of the phase difference is reduced by  $1 - \text{sinc}((\Delta\phi)_{\max}/2)$ , where  $\text{sinc}(x) = \sin(x)/x$ . For a maximum SNR reduction of 5%, the total sidereal phase change during the integration must be  $<1.1$  rad. For this experiment, the sidereal change during the nominal 4-s coherent integration time is much less than this value. However, due to occasional loss of lock and the time required for fringe reacquisition, data is not recorded at a 100% duty cycle, and the actual time required to obtain 1000 frames can exceed 4 s. Consequently, we edited out those points whose duration was such that the constraint above on sidereal motion during the integration time was exceeded. While it would be straightforward to incorporate the sidereal motion into the phase-reference calculation to allow for arbitrary coherent integration times, the fraction of rejected points was  $<0.5\%$ , so this step was not taken. Finally, one 6- $\sigma$  outlier was deleted from segment C. No further editing was performed. Column 5 of Table 1 gives the number of 1000-frame points (henceforth 4-s points) per segment analyzed in detail below.

For each data segment, a best-fit sidereal sinusoid was subtracted from the 4-s points, and the Allan variance of the residuals was calculated as in Sect. 5.1. The Allan standard deviations at 4 s (i.e., the first Allan point) are recorded in col. 11 of Table 2. Concurrent with the phase-difference calculation, the signal-to-noise ratio of the phase-difference estimator and the cross coherence were calculated as described in the appendix. These quantities are included in cols. 8 and 9 of Table 2; col. 10 gives the predicted photon-noise contributions to the residuals corresponding to the phase-difference SNR. Column 12 of Table 2 gives the Allan deviations of the residuals corrected for the photon-noise bias; in principle, these corrected values represent the atmospheric noise only. For all of the observations presented here, the projected interferometer baseline was within 0.4% of its 12.0-m physical length. Using this value to convert the phase differences to angle, and hypothesizing white-noise behavior, yields the last column of Table 2, which expresses the photon-noise-corrected deviations in terms of  $\mu\text{as}$  astrometric error per  $\sqrt{t}$  integration time.

## 5. Discussion

### 5.1. Shape of the phase-difference power spectrum

One of the goals of this investigation was to verify that the power spectrum of the phase difference is white, as predicted, allowing for a  $\sqrt{t}$  improvement in astrometric accuracy with increasing integration time. Thus we computed for each segment the Allan variance (cf. Thompson et al. 1986) from the 4-s residuals  $x_i$ . The Allan variance  $\sigma_{x,A}^2$  at lag 1 ( $l \geq 1$ ) was calculated as

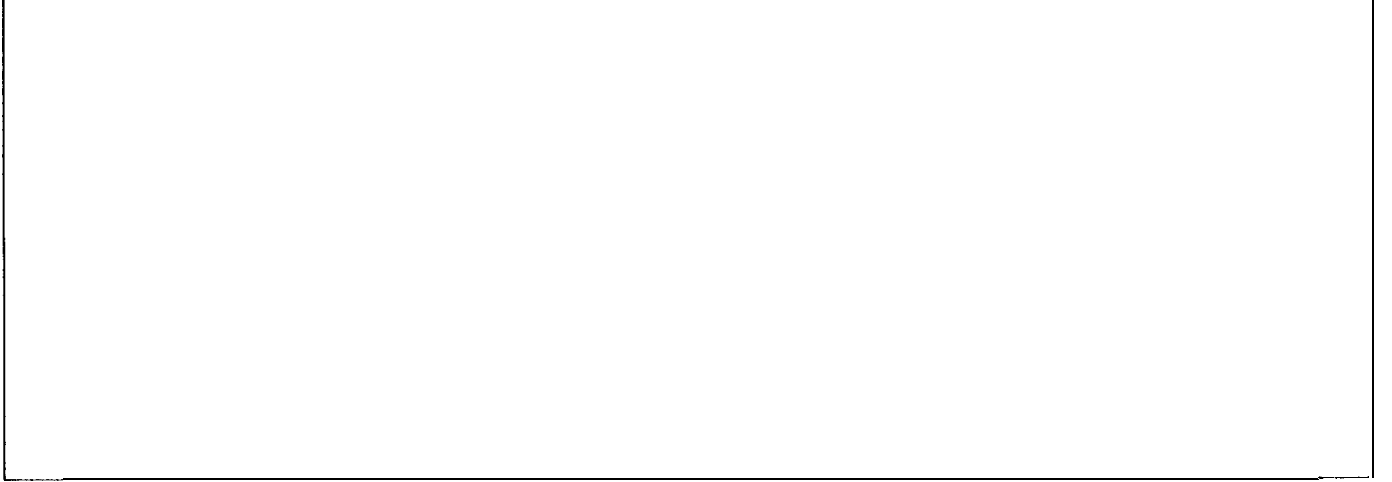
$$\sigma_{x,A}^2 = \frac{1}{2(M'+1-2l)} \sum_{n=0}^{M'-2l} \left( \frac{1}{l} \sum_{m=0}^{l-1} x_{n+m} - x_{n+l+m} \right)^2, \quad (7)$$

where  $M'$  is the total number of points. For this calculation the data points in each segment were simply concatenated without time-tagging, i.e., they were assumed evenly spaced at 4-s intervals. Because of irregular sampling, discussed above, this has the effect of slightly blurring any narrow spectral features which may exist in the data, but would not obscure trends indicative of non-white behavior. The Allan-variance points were corrected for photon-noise bias using the values given in col. 10 of Table 2 as  $(\sigma_{x,A}^2)^c(l) = \sigma_{x,A}^2(l) - \sigma_{\text{PN}}^2/l$ . The square roots of the uncorrected and corrected Allan variances for  $l=1$  are the values given in cols. 11 and 12 of the table.

Inspection of the Allan variances at this stage revealed a broad spectral feature for certain of the segments at an integration time corresponding to the mean fringe-wrap period (cf. Fig. 4). This feature was identified as leakage of the bright primary into the tails of the secondary narrowband coherence function, which is consistent with the observation that the strength of the feature was largest for those segments with the smallest differential delay.<sup>2</sup> Thus, assuming constant primary leakage for each segment, we subtracted a best-fit sinusoid at the wrap rate from each data set and recomputed the Allan variances with the bias correction. Figure 5 plots the Allan deviations vs. integration time for the six segments analyzed here. The spacing of data points is 4 s. The maximum integration time plotted was limited to that which yielded 4 independent terms in the outer average of the Allan-variance calculation (i.e.,  $1 < M'/5$ ), at which point the SNR per point (assuming a white-noise spectrum) was  $\sim 1.2$ . The Allan deviation of a white-noise process exhibits  $\sqrt{t}$  behavior, illustrated by the solid lines in the figure. Over the time duration shown in the plot, which extends to  $t \sim 8$  rein, the atmospheric residuals are consistent with the predicted white-noise behavior.

<sup>2</sup>If for some reason the effective pathlength-modulation stroke were mismatched to the wavelength, it would also introduce a phase-measurement error periodic with the wrap rate. However, this error would be at the second harmonic of the wrap rate (Colavita et al. 1987), while the spectral feature we see is at the fundamental, with negligible second-harmonic content.

Fig. 5. Allan deviations for the six segments as a function of time after subtraction of the primary leakage. These values have been corrected for the photon-noise bias. The plotting interval is nominally 4 s (see text). The solid lines, which illustrate  $\sqrt{t}$  behavior, are the predictions from the two models discussed in Sect. 5.3.



### 5.2. Photon-noise floor and performance of the phase-difference estimator

Two calibration data sets were analyzed to examine the system noise floor and phase-difference estimator performance. These are identified as segments C1 and C2 in Tables 1 and 2, which include the relevant observational and measurement parameters for these data. For these segments the differential delays were set so that both channels measured the phase of the primary star. For segment C1 the differential delay was set near zero to yield a strong signal in both channels; for segment C2 the delay was set somewhat away from zero to yield only a weak primary signal in the secondary channel. Segment C1 establishes an upper bound on the systematic noise floor of this experiment. For this high-SNR case the rms of the residuals falls a factor of two below the smallest rms measured for data sets A-F. Clearly, the fact that the Allan variances do not exhibit non-white behavior at large lags also indicates that the system noise floor is lower than the atmospheric noise floor over the time scales of this experiment.

Segment C2 serves as a test of the accuracy of the predicted photon-noise bias which is subtracted from the data sets above. With its low SNR, the rms of its residuals is much higher than for C1 and is dominated by the photon noise of the phase-difference estimator. However, subtracting the predicted photon-noise variance yields a corrected residual which is still larger than for C1. This implies that the predicted photon-noise bias calculated from the estimated phase-difference SNR may slightly underestimate the true bias. Thus the bias corrections applied to segments A-F should be conservative. If the bias corrections applied to the segments were scaled such that the corrected residuals for C1 and C2 were the same (a scaling of 20% in the standard deviation  $\sigma_{PN}$ ), the mean astrometric error for the 6 data sets would be reduced 10%.

There are some additional points worth commenting on regarding these two data sets. As the pupils used for the two channels are separated spatially, the residuals of the phase difference will remain nonzero even though both channels are observing the same source. The size of this term is readily calculated. Starting with Eq. (1), we substitute  $d$ , the mean separation of the two beams, for  $0h$ , and convert to fringe position by multiplication by  $B^2$ , yielding

$$\epsilon_{\Delta x}^2 = 5.25 B^{2/3} d^2 \int dh C_n^2(h) W^{-1}(h) t^{-1}, \quad t > B/W, \quad (8)$$

or, with  $W(h) = W$ , this expression can be written in terms of  $r_0 = 1.68 [k^2 \int dh C_n^2(h)]^{-3/5}$  as

$$\epsilon_{\Delta x}^2 = 12.5 k^{-2} B \left( \frac{d}{B} \right)^{1/3} \left( \frac{d}{r_0} \right)^{5/3} (Wt)^{-1}, \quad t > B/W. \quad (9)$$

For this experiment the mean separation between beams  $d$  is 2.5 cm (the smoothing caused by the finite pupil extent affects only the high-frequency portion of the power spectrum and thus doesn't play a role in this calculation). Substituting  $r_0 = 21$  cm at  $\lambda = 0.55$  (calculated below), and  $W = 10$  ln/s, a typical value, yields  $\epsilon_{\Delta x} = 0.010$  pm rms at  $t = 4$  s, which is consistent with the 0.014 pm rms computed for segment C1.



The other point relates to the cross coherence  $\Gamma_d^2$ . If we let  $\sigma_{\Delta\phi}^2$  be the variance of the phase-difference fluctuations during the coherent integration time - we assume that the coherent integration time is long enough that the full variance, rather than a high-pass-filtered version, is appropriate - then  $\Gamma_d^2$  is given by

$$\Gamma_d^2 = \exp(-\sigma_{\Delta\phi}^2), \quad (10)$$

as discussed in the appendix. For two rays separated by distance  $d$ , the variance is given by the standard result (cf. Roddier 1981):  $\sigma_{\Delta\phi}^2 = 2 \times 6.88(d/r_0)^{5/3}$ , where the factor of 2 accounts for assumed independent contributions from each aperture, a good approximation when  $B \gg r_0$ . With  $d = 2.5$  cm and  $r_0(700 \text{ nm}) = 28$  cm,  $\sigma_{\Delta\phi}^2 = 0.25 \text{ rad}^2$ . In reality, there will be substantial aperture smoothing of the variance due to the finite aperture extent. For the geometry of this experiment we estimate the aperture smoothing to be 0.60, yielding a corrected variance of  $\sigma_{\Delta\phi}^2 = 0.15 \text{ rad}^2$ . The cross coherence attributable to this value is 0.86, which is much higher than the 0.45-0.48 observed for segments C1 and C2.

The hypothesis for the additional coherence reduction on the calibration segments is that residual guiding errors are being manifest as OPD errors due to the use of off-axis apertures. Guiding errors of  $0.5''$  rms at each aperture in the axis of the beam separation would contribute an additional  $0.6 \text{ rad}^2$  of phase variance, which with the contribution above would account for the observed cross coherence.<sup>3</sup> This seems a reasonable explanation, especially as the partial intrusion of the delay plate and mount into the angle-tracking annulus would degrade guiding along the separation axis.

### 5.3. Correlation of the measurements with atmospheric models

Beyond verification of a white-noise spectrum for the differential residuals, the other objective of this experiment was to compare the size of the residuals with the theoretical predictions. Thus some seeing measures are needed to supply the parameters for Eq. (1). One straightforward seeing measure is the rms OPD fluctuations  $\sigma_x$  of a single star, which are readily calculated from the laser-monitored delay-line positions, recorded at a 4-ms rate, after subtraction of the sidereal term. These values are given in col. 7 of Table 1.<sup>4</sup> Each has been scaled by  $\sim 5\%$  to account for the high-pass filtering of the finite segment length  $T$ . The scaling (for standard deviation) is given as  $1/[1 - 0.63(B/(WT))^{1/3}]$ , which can be derived from the expression for the power spectrum of the phase fluctuations (cf. Colavita et al. 1987). These fluctuations relate to  $r_0$  as  $\sigma_x^2 = 6.88k^{-2}(B/r_0)^{5/3}$ . Using this expression estimated values for  $r_0$ , at a nominal wavelength of  $0.55 \mu\text{m}$ , and seeing  $\lambda/r_0$ , are given in cols. 9 and 10 of Table 1. These are the as-measured quantities, uncorrected for zenith angle (given in col. 7 of the table). The mean value of  $r_0$  for segments A-F is 21 cm at  $0.55 \mu\text{m}$  - 28 cm at the observation wavelength of 700 nm - for mean seeing of  $\sim 0.54''$ .

While a useful measure of the overall seeing,  $r_0$  alone is deficient in predicting the astrometric error in a differential measurement. As seen from Eq. (1), the astrometric error depends on an integral of the turbulence profile which emphasizes the upper atmospheric layers, while  $r_0$  is a function of an integral of an unweighted turbulence profile. As an additional atmospheric measure we can consider the isoplanatic angle, given by  $\theta_0 = 0.31(r_0/h_{5/3})$ , where  $h_{5/3} = [\int C_n^2 h^{5/3} dh / \int C_n^2 dh]^{3/5}$  (Roddier et al. 1982). This weighting is much closer to that used in calculating the astrometric error, and should be a better performance predictor, for an interferometer with independent contributions from each aperture, the phase-difference variance as a function of star separation  $\theta$  is given by

$$\sigma_{\Delta\phi}^2 = 2(\theta/\theta_0)^{5/3} + \sigma_0^2, \quad (11)$$

where the term  $\sigma_0^2$  represents the additional fluctuations identified above ( $\sim 0.6 \text{ rad}^2$ ). This expression is clearly an approximation for this experiment with spatially separate, finite-extent apertures. However, with a  $3.3''$  star separation, the linear separation at, say, 10 km, will be 16 cm, which is much larger than the 2.5-cm beam separation on the ground. In addition, the spatial separation, which will tend to increase the variance, will be offset by the aperture averaging of the finite apertures, which will tend to decrease the variance, so that the simple expression above should be a good approximation.

Similar to the analysis in Sect. 5.2, we can estimate the isoplanatic angle using Eqs. (11) and (10). The results, scaled to  $0.55 \mu\text{m}$ , are given in col. 10 of Table 1; the mean value is  $2.9''$ . Comparison of the final results for astrometric

<sup>3</sup> As a check, we calculated the cross coherence between the primary narrowband and white-light channels. The measured value for the section of data analyzed was 0.85, which is reasonable given the systematic phase-measurement errors which occur in the white-light channel because of the wide spectral bandwidth and because of mismatches between the assumed and actual effective wavelength (which is especially important when fringe hopping occurs).

<sup>4</sup> For the short segment C1,  $\sigma_x$  was estimated from an adjacent 20-min section of data beginning at 5<sup>h</sup> 93.

Table 3. Summary of atmospheric parameters

model/observation	$r_0$ (0.55 $\mu\text{m}$ )	$\theta_0$ (0.55 $\mu\text{m}$ )	$\epsilon_{\Delta\theta}$ (arc sec)	$\epsilon_{\Delta\theta}(B = 12 \text{ m}, \theta = 3.3'')$ ( $\mu\text{as}/\sqrt{h}$ )
Hufnagel model	12 cm	1.3''	$540B^{-2/3}\theta t^{-1/2}$	27
Mauna Kea model	21 cm	3.5''	$300B^{-2/3}\theta t^{-1/2}$	15
Current observations (mean)	21 cm	2.9''		21

error (col. 13, Table 2) with the values of  $r_0$  and  $\theta_0$  shows better correlation of the error with isoplanatic angle than with coherence diameter.

Two numeric evaluations of Eq. (1) were presented by Shao & Colavita (1992). One was that computed by Lindgren (1980) for the case of a Hufnagel turbulence profile with a standard wind model, while the other used measured turbulence and wind-velocity profiles from a seeing campaign at Mauna Kea (Roddier et al. 1990). The predictions of the Hufnagel and Mauna Kea models for the star separation and baseline of this experiment, 27 and 15  $\mu\text{as}/\sqrt{h}$ , resp., are plotted as the upper and lower solid lines in the Allan variance plot, Fig. 5. The measured errors range from 15 to 25  $\mu\text{as}/\sqrt{h}$ , with a mean value of 21  $\mu\text{as}/\sqrt{h}$ . The mean values of astrometric error,  $r_0$ , and  $\theta_0$  for this experiment are summarized in Table 3 along with the predictions of the theoretical models and the seeing parameters of the assumed profiles.

From the table the atmospheric parameters for the measured data are seen to be similar to those of the Mauna Kea model, but with a slightly smaller isoplanatic angle. For a uniform scaling of the turbulence profile  $C_n^2(h)$ , the astrometric error scales with isoplanatic angle as  $\theta_0^{-5/6}$ . Scaling the astrometric error for the Mauna Kea profile to the measured isoplanatic angle yields a prediction of 18  $\mu\text{as}/\sqrt{h}$ . While, as discussed above, the isoplanatic angle is not a complete predictor of astrometric performance, the measured 21  $\mu\text{as}/\sqrt{h}$  is remarkably close to this value. In addition, both the likelihood of an underestimate of the photon-noise bias, discussed above, as well as the generally more element winds at Mt. Wilson than at Mauna Kea, would tend to improve the agreement between theory and measurement. To make a more rigorous comparison would require detailed simultaneous turbulence-profile and wind-speed measurements. However, on the basis the data at hand, the measured values seem in good agreement with the theoretical predictions.

#### 5.4. Astrometry of $\alpha$ Gem

Although not the objective of this investigation, the measurements made here allow for an accurate determination of the separation of  $\alpha$  Gem A-II at this epoch. The binary separation  $\Delta\delta$ , Acr is related to the differential delay  $\Delta x(t)$  through Eq. (4). As the fixed delays introduced by the rotating plate were not known precisely, the astrometry used only the  $\sin H$  and  $\cos H$  terms in that expression. More precisely, the 6 data segments were used together in a single least-squares solution for 8 parameters: the coefficients of the  $\sin$  and  $\cos$  terms of the sidereal delay along with 6 constant terms. Using these coefficients yields a solution for  $\Delta\delta$  and  $\Delta\alpha$  of 0.947'' and 3.700'', or in terms of separation and position angle, 3.281'' and 73.23°. While the formal errors for separation and position angle are small: 0.002'' and 0.07°, they would be much smaller in a practical narrow-angle instrument which included metrology of the differential delay to allow for a solution from the delay, rather than from what is essentially the delay rate; an orthogonal baseline would also provide improved two-dimensional astrometry.

The major systematic effect which degrades accuracy is the knowledge of the narrowband filter's center wavelength, specified by the manufacturer as  $\pm 3.5$  nm; this uncertainty should not effect the position angle. The other systematic effects considered seem small: baseline knowledge is  $\sim 10$  pm; differential refraction (which involves only the second-order refraction term, as the vacuum delay lines of the Mark III eliminate the first-order term) is calculated to be  $< 1$  pas; the shift of the effective wavelength of the narrowband channels due to the spectral slope of the source across the bandpass is much smaller than the manufacturing uncertainty mentioned above; and the linear approximation used in Eq. (4) introduces errors smaller than 10 pas. If required, these effects could be reduced by modeling, calibration, or nonlinear analysis. Clearly, a long-term observing program is needed to validate the formal errors given above. For now, we will conservatively double the formal errors and add in the filter uncertainty (interpreted at  $\pm 2\sigma$ ) to yield separation, position angle, and 1- $\sigma$  errors for  $\alpha$  Gem at 1992.9589 of  $3.281'' \pm 0.01''$  and  $73.23^\circ \pm 0.15^\circ$ .

## 6. Conclusion

The predictions for the astrometric error in a differential measurement of closely-spaced stars made with a long-baseline interferometer are quite small. Measurements with the Mark III interferometer have been conducted to verify some of the predictions of the theoretical models. For a star separation of 3.3" and a baseline of 12 m, the measured residuals correspond to an astrometric error of  $21 \mu\text{as}/\sqrt{h}$ , which is in good agreement with the predictions of the models. The Allan variance of the data is consistent with white-noise behavior out to an integration time of 8 min, a time which was limited by the length of the available data segments. While these measurements clearly cannot state that the error is white at longer integration times, we see no evidence of anomalous behavior at the shorter time scales which would pose problems at longer integration times.

A more complete understanding of the atmospheric limits to narrow-angle interferometric astrometry over a range of star separations, baselines, and integration times, with adequate sensitivity to observe a large number of sources, requires an instrument optimized for narrow-angle measurements. This optimization includes larger apertures, a dual-star feed at each aperture, separate beam trains, infrared operation, and complete metrology of the optical path. The NASA TOS (Toward Other Planetary Systems) program has recently funded development of the TOPS Interferometer Technology Testbed, an instrument which includes these optimizations. The goal of this instrument is to verify the atmospheric limits and demonstrate the technology needed to achieve narrow-angle differential astrometric accuracies of tens of microarcseconds. With such accuracy one could conduct an extensive search for Jupiter- and Saturn-mass planets around thousands of stars, as well as for Uranus-mass planets around >50 stars.

**Acknowledgements.** Thanks to M. Shao, X. P. Pan, and S. B. Shaklan for their assistance, and to C. A. Hummel, C. S. Denison, and L. W. Rarogiewicz for help with the observations. This work was performed at the Jet Propulsion Laboratory, California Institute of Technology, under a contract with the National Aeronautics and Space Administration.

### A. Signal-to-noise ratio of the phase difference

As the signal-to-noise ratio in a single frame is too small for an unbiased calculation of the phase difference, the difference phasor is first integrated over  $M$  frames. Let  $X_{ij}, Y_{ij}$  be the quadratures of the raw phasors for star  $i, i = 1, 2$ , for frame  $j$ . The quadratures  $X_d, Y_d$  of the difference phasor are calculated as

$$\begin{aligned} X_d &= \sum_{j=1, M} X_{1j} X_{2j} + Y_{1j} Y_{2j} \\ Y_d &= \sum_{j=1, M} X_{1j} Y_{2j} - Y_{1j} X_{2j} \end{aligned} \quad (\text{A1})$$

The difference phase  $\Delta\phi$  is calculated from the integrated phasors as

$$\Delta\phi = \arctan\left(\frac{Y_d}{X_d}\right). \quad (\text{A2})$$

The raw quadratures for the two stars have means (cf. Walkup & Goodman 1973)

$$\begin{aligned} \bar{X}_i &= \frac{\sqrt{2} N_i V_i}{\pi} \cos \phi_i \\ \bar{Y}_i &= \frac{\sqrt{2} N_i V_i}{\pi} \sin \phi_i, \end{aligned} \quad (\text{A3})$$

where  $N_i, V_i$ , and  $\phi_i$  are the mean photon rate per frame, the fringe visibility, and the instantaneous fringe phase; the factor  $\sqrt{2}/\pi$ , rather than  $1/2$ , arises from the use of 4 discrete time bins during demodulation. The mean-square values of the raw quadratures are given by

$$\begin{aligned} \overline{X_i^2} &= \bar{X}_i^2 + N_i/2 \\ \overline{Y_i^2} &= \bar{Y}_i^2 + N_i/2. \end{aligned} \quad (\text{A4})$$

As the raw quadratures are statistically independent, the means of the difference quadratures are given by

$$\begin{aligned} \bar{X}_d &= \frac{2}{\pi^2} M N_1 V_1 N_2 V_2 \Gamma_d \cos \Delta\phi \\ \bar{Y}_d &= \frac{2}{\pi^2} M N_1 V_1 N_2 V_2 \Gamma_d \sin \Delta\phi, \end{aligned} \quad (\text{A5})$$

where  $\Delta\phi$  is the average phase difference over the coherent integration time and  $\Gamma_d^2$  is the cross coherence of the two phases, viz.  $\Gamma_d^2 = \text{Cxp}(-\text{trio})$ , where  $\sigma_{\Delta\phi}^2$  is the variance of the phase difference, assumed Gaussian, during the coherent integration time.

Using Eq. (A1) and the independence of the raw quadratures, the mean square of  $X_d$  is given by

$$\begin{aligned}\overline{X_d^2} &= M\overline{X_1^2 X_2^2} + M(M-1)\overline{X_1^2 X_2^2} \\ &+ M\overline{Y_1^2 Y_2^2} + M(M-1)\overline{Y_1^2 Y_2^2} \\ &+ 2M^2\overline{X_1 X_2 Y_1 Y_2}.\end{aligned}\quad (\text{A6})$$

Substituting Eq. (A4) yields

$$\begin{aligned}\overline{X_d^2} &= \frac{1}{2}MN_1(\overline{X_2^2} + \overline{Y_2^2}) + \frac{1}{2}MN_2(\overline{X_1^2} + \overline{Y_1^2}) \\ &+ \frac{1}{2}MN_1N_2 + M^2(\overline{X_1 X_2} + \overline{Y_1 Y_2})^2.\end{aligned}\quad (\text{A7})$$

Finally, substituting Eqs. (A1) and (A3) yields

$$\begin{aligned}\overline{X_d^2} &= \frac{1}{2}MN_1\frac{2(N_2V_2)^2}{\pi^2} + \frac{1}{2}MN_2\frac{2(N_1V_1)^2}{\pi^2} \\ &+ \frac{1}{2}MN_1N_2 + \overline{X_d^2},\end{aligned}\quad (\text{A8})$$

and thus the variance of  $X_d$  is given by the first three terms of this expression. The variance of  $Y_d$  is identical, and both are denoted as  $\sigma_d^2$ . The SNR is defined traditionally as the mean length of the phasor divided by the standard deviation of the orthogonal noise term, viz.  $\text{SNR}_d^2 = S_d^2 = \overline{p_d^2}/\sigma_d^2$ . Let

$$S_i^2 = \frac{4}{\pi^2}N_iV_i^2 \quad (\text{A9})$$

be the square of the high-light-level signal-to-noise ratio for the individual phases. The square of the mean phasor length  $\overline{p_d}$  can be written

$$\overline{p_d^2} = \frac{1}{4}M^2N_1N_2S_1^2S_2^2\Gamma_d^2, \quad (\text{A10})$$

and the square of the difference-phase SNR is thus given by

$$S_d^2 = \frac{\frac{1}{2}MS_1^2S_2^2\Gamma_d^2}{1 + \frac{1}{2}(S_1^2 + S_2^2)}. \quad (\text{A11})$$

This expression has intuitive asymptotic forms. Assume  $S_1 = S_2$ . When photon-rich, the SNR of the difference is just  $S_d = \sqrt{M}\Gamma_d S_1/\sqrt{2}$ , which is what would be expected from the difference of the two phases; when photon-starved, the SNR becomes dependent on  $N^2$  rather than  $N$ , viz.  $S_d = \sqrt{M}\Gamma_d S_1^2/\sqrt{2}$ .

For the data analyzed in this paper, the SNR in the narrowband primary channel is  $\gtrsim 1$ , so there is little penalty in essentially using it as the phase reference. However, were both narrowband SNRs less than unity, a better SNR for the phase difference would result from phase referencing the narrowband channels to the phase of the wideband channel.

Using Eqs. (A9) and (A10), an estimator for the cross coherence is given by

$$\widehat{\Gamma_d^2} = 4 \frac{(X_d^2 + Y_d^2) - MN_1N_2(1 + \frac{1}{2}(S_1^2 + S_2^2))}{M^2N_1N_2S_1^2S_2^2}. \quad (\text{A12})$$

## References

- Colavita M.M., Shao M., Staelin D.H., 1987, Appl. Opt. 26, 4106  
 Gatewood G., 1991, BAAS 23, 1433  
 Han I., 1989, AJ 97, 607  
 Hirshfeld A., Sinnott, R. W., 1985, Sky Catalogue 2000.0. Cambridge Univ. Press, Cambridge  
 Lindegren L., 1980, A&A 89, 41  
 Roddier F., 1981, The Effects of Atmospheric Turbulence in Optical Astronomy. In: Wolf E. (ed.) Progress in Optics XIX. North-Holland, Amsterdam, p. 281  
 Roddier F., Cowie I., Graves J. E., Songaila A., 1990, Proc.SPIE 1236, 485  
 Roddier F., Gilli J. M., Vernin J., 1982, J. Opt. (Paris) 13, 63  
 Shao M., Colavita M.M., 1992, A&A 262, 353  
 Shao M., Colavita M. M., Hines B. E., et al., 1988a, A&A, 193, 357  
 Shao M., Colavita M. M., Hines B. E., et al., 1988b, ApJ 327, 90.5  
 Thompson A.R., Moran J.M., Swenson G. W. Jr., 1986, Interferometry and Synthesis in Radio Astronomy. Wiley, New York  
 Walkup J. F., Goodman J. W., 1973, J. Opt. Soc. Am. 63, 399

This article was processed by the author using Springer-Verlag L<sup>A</sup>T<sub>E</sub>X A&A style file L-AA version 3.

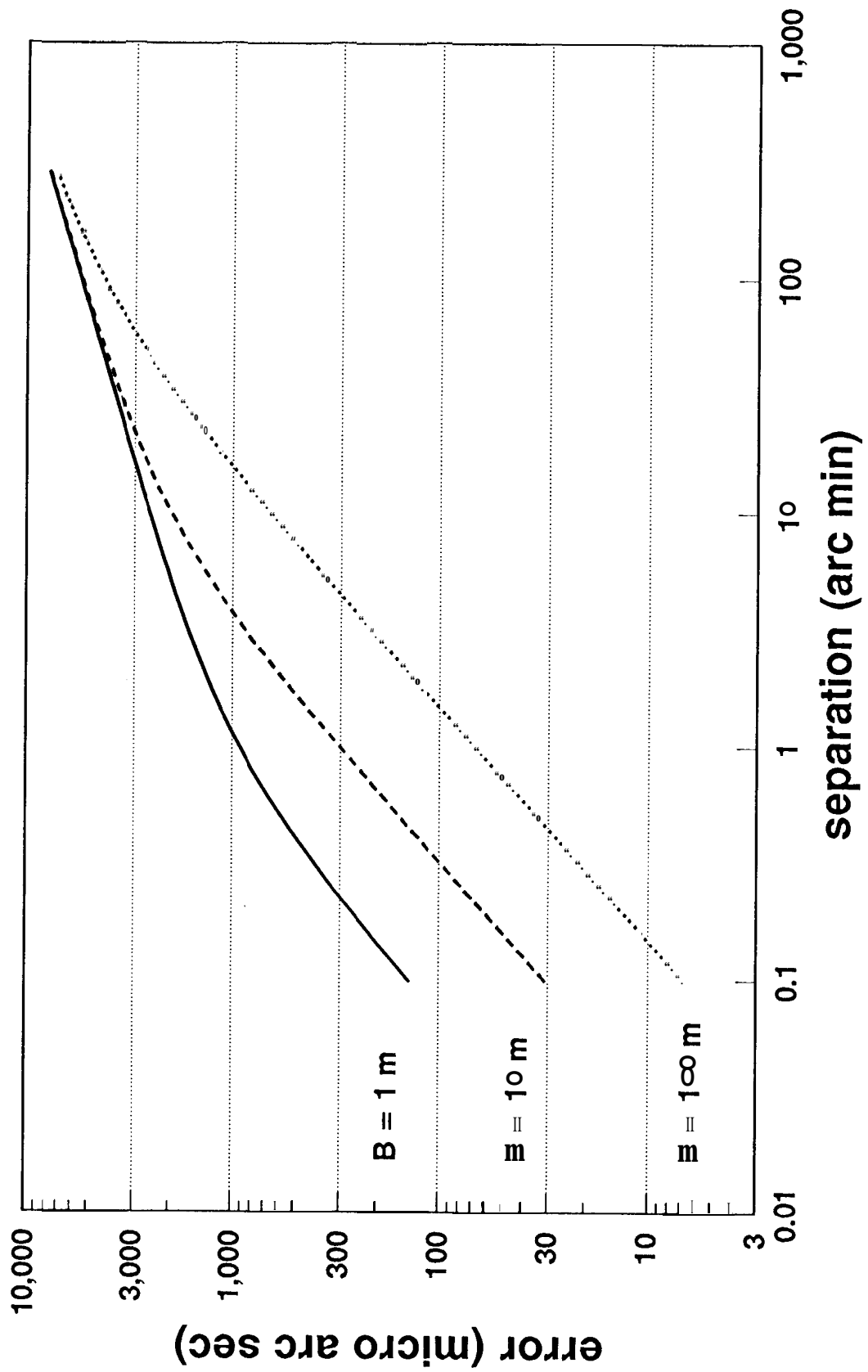


Fig 1

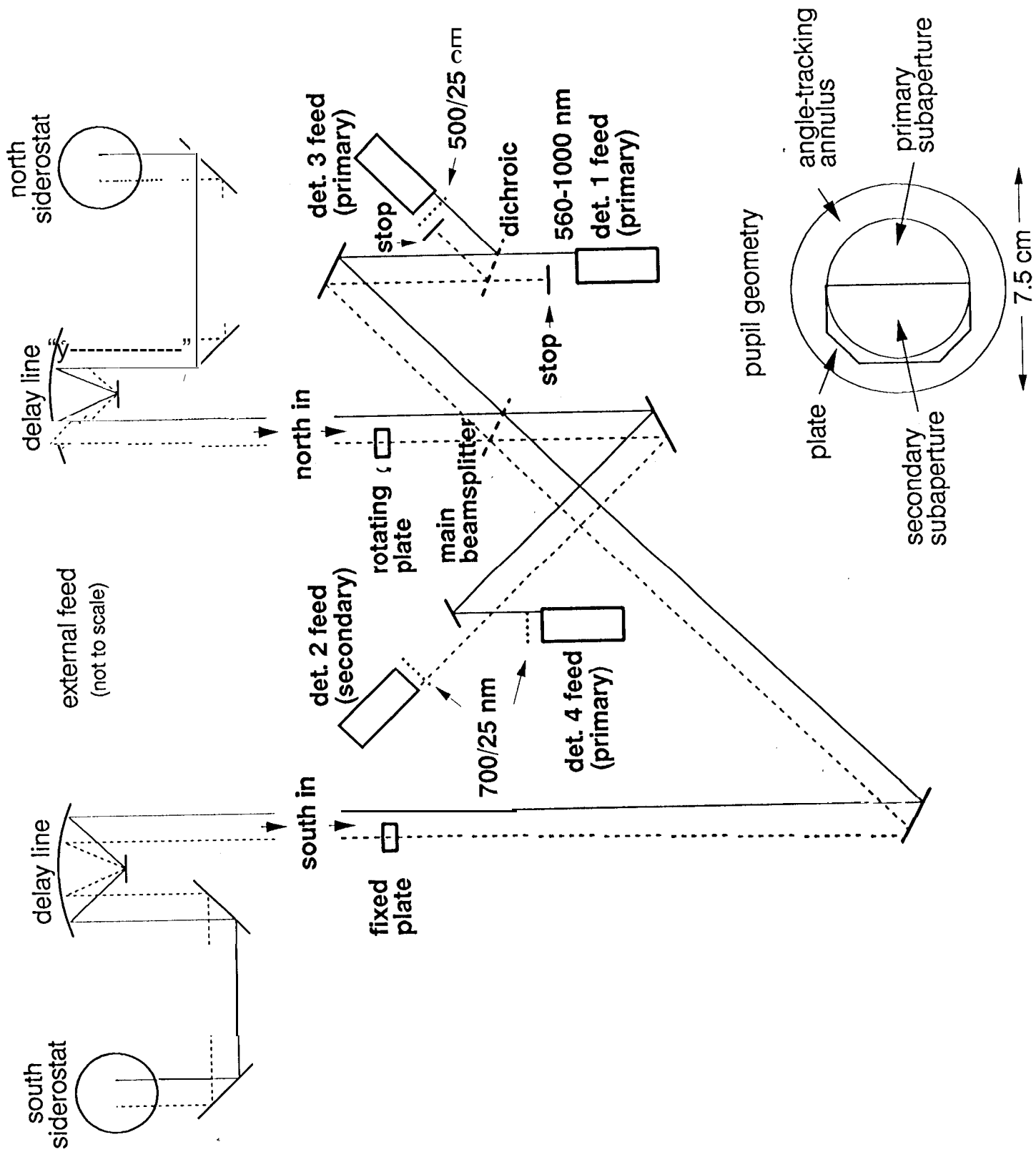
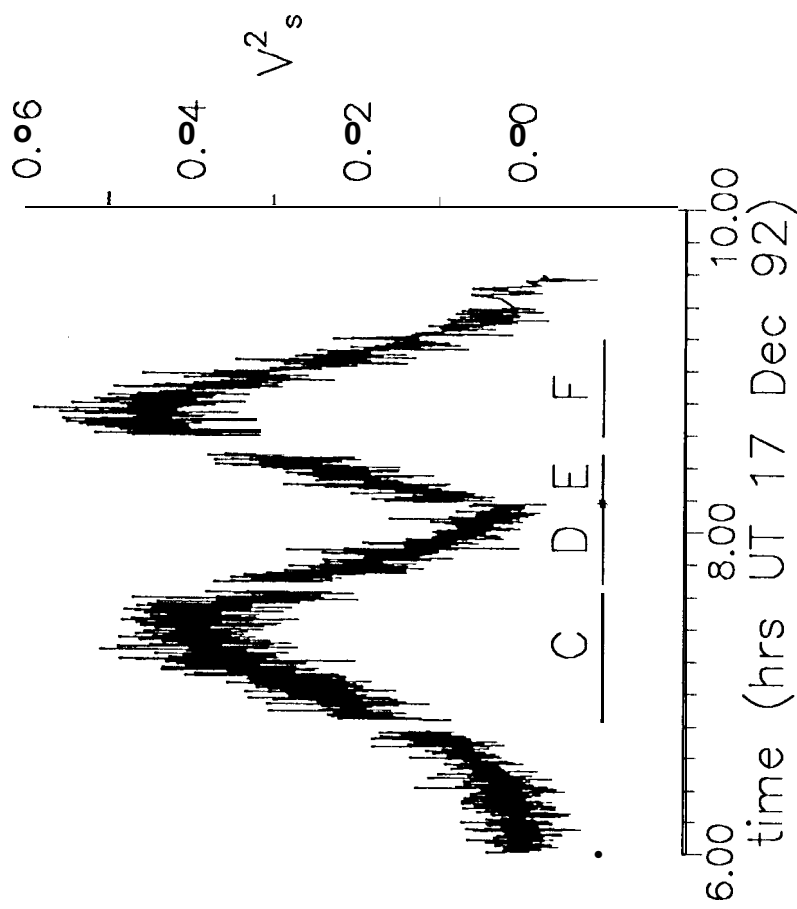
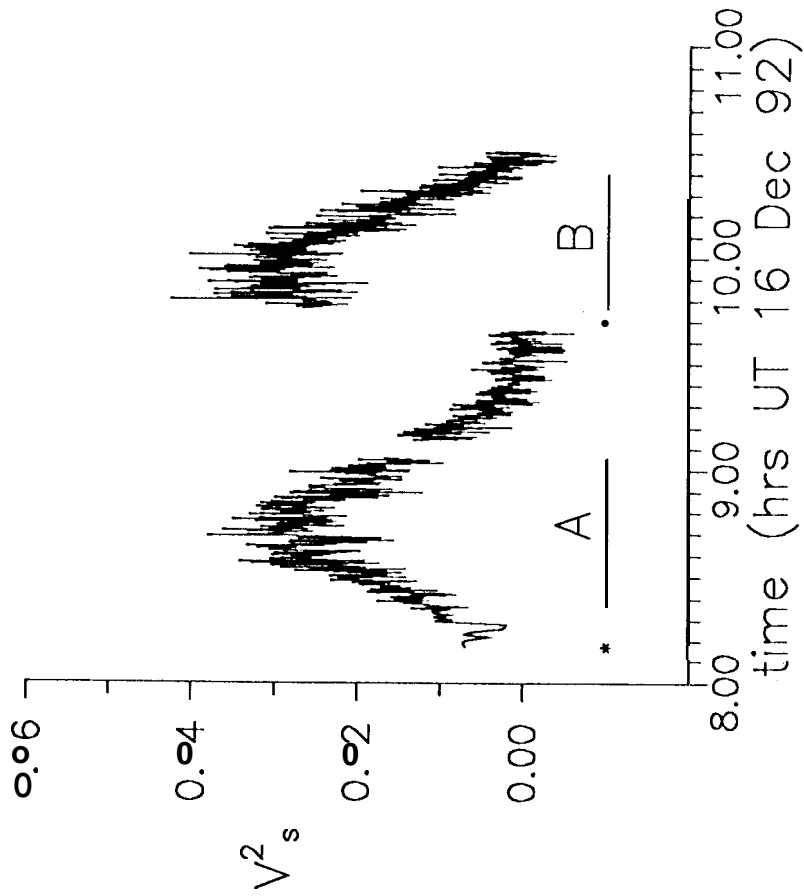


Fig 2



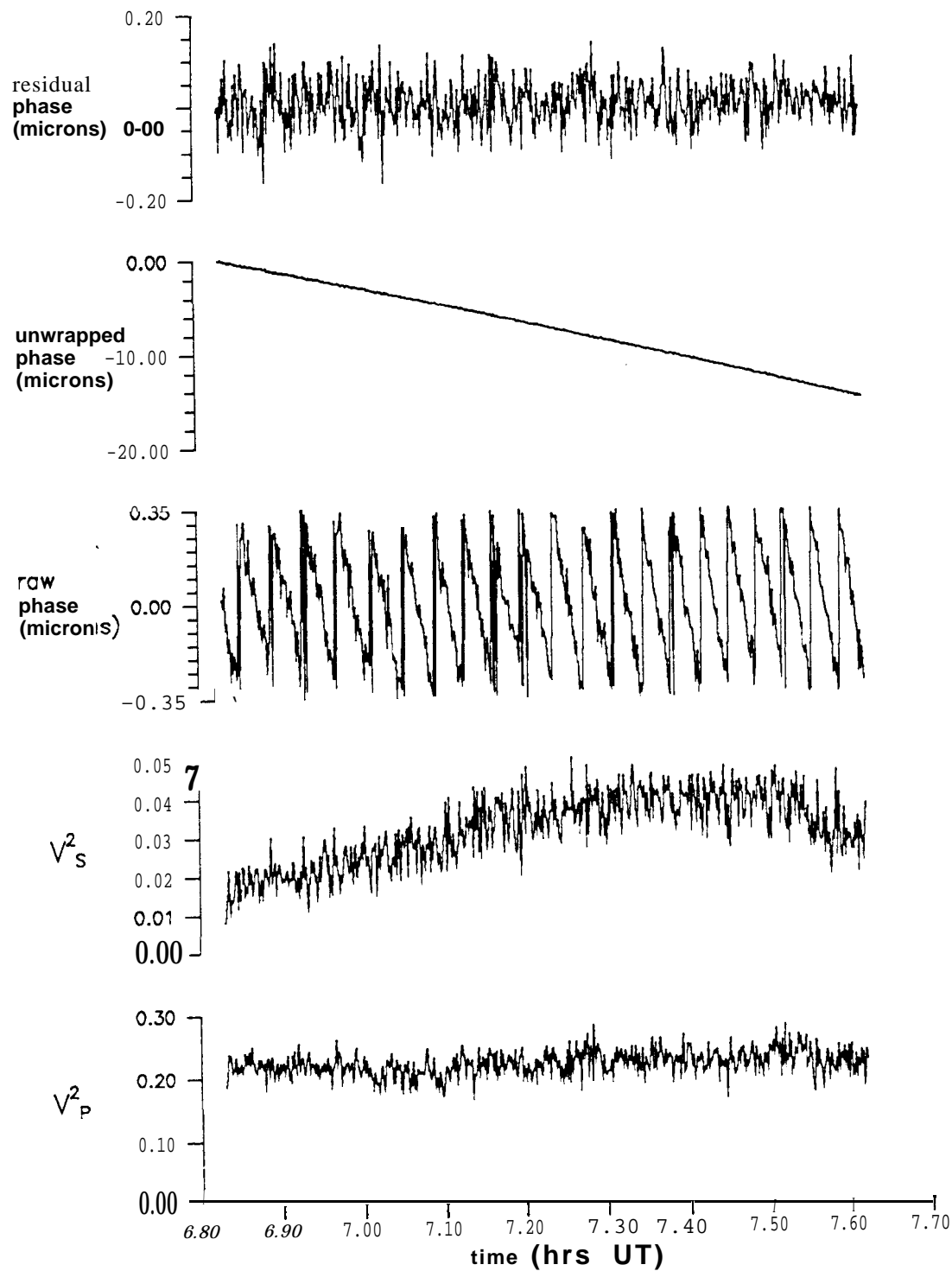


fig 4



